Check for updates

Oil palm leaf-derived hierarchical porous carbon for "water-in-salt" based supercapacitors: the effect of anions (Cl⁻ and TFSI⁻) in superconcentrated conditions†

Arisa Phukhrongthung,[a] Pawin Iamprasertkun, [ID] [b] Aritsa Bunpheng,[b] Thanit Saisopa,[c] Chakkrit Umpuch,[d] Channarong Puchongkawarin,[d] Montree Sawangphruk [ID] [e] and Santamon Luanwuthi [ID] *[a]

This study investigates the use of a hierarchical porous carbon electrode derived from oil palm leaves in a "water-in-salt" supercapacitor. The impact of anion identity on the electrical performance of the carbon electrode was also explored. The results show that the prepared carbon had a hierarchical porous structure with a high surface area of up to 1840 m² g⁻¹. When a 20 m LiTFSI electrolyte was used, the carbon electrode had a specific capacitance of 176 F g⁻¹ with a wider potential window of about 2.6 V, whereas the use of a cheaper 20 m LiCl electrolyte showed a higher specific capacitance of 331 F g⁻¹ due to the smaller size of the Cl⁻ anion, which enabled inner capacitance. Therefore, the anion identity has an effect on the electrochemical performance of porous carbon, and this research contributes to the understanding of using "water-in-salt" electrolytes in carbon-based supercapacitors. The study's findings provide insights into developing low-cost, high-performance supercapacitors that can operate in a wider voltage range.

1. Introduction

Supercapacitors, a class of electrochemical energy storage devices, have attracted tremendous interest due to their high-power density (4000–10 000 W kg⁻¹), excellent cycle stability (50 000–100 000 cycles), good reversibility and low maintenance.[1–4] They have great potential for use in a wide range of applications such as electric vehicles, portable electronics and high-power tools.[2,5,6] However, the poor energy density (1–10 W h kg⁻¹) of supercapacitors hinders their practical applications.[3,4,7] Therefore, increasing the energy density of supercapacitors is a key challenge. Principally, the supercapacitor is categorised into double-layer capacitors (EDLCs) and pseudocapacitors. EDLC materials generally store energy

electrostatically by the adsorption of the ions at the electrode/electrolyte interface, while electrical energy is stored in pseudocapacitor materials through a faradaic reaction at the surface (also refer to the ions intercalation[8]). Although the EDLC possess a low energy density compared to the pseudocapacitor, it exhibits superior rate capability and cycling stability.[7,9,10] Still, the performance of the supercapacitor in both categories mainly depends on electrode materials and the type of electrolytes.[7,11]

Carbon-based materials have been promising materials for EDLC owing to their large surface area (1000–3500 m² g⁻¹),[4,12] good electrical conductivity (up to 10⁶ S m⁻¹ depending on the carbon structures),[12–14] and excellent chemical stability.[10,15] Various carbonaceous materials such as carbon nanotubes,[16–18] porous carbon,[19,20] and graphene[21,22] have been intensively developed in the past few years. Among these, porous carbon shows exceptional characteristics such as high accessible surface area and short diffusion pathways, which could be advantageous for improving the capacitance and rate capability of supercapacitors.[20,23] In general, hierarchical porous carbon usually contains at least two kinds of pores; that is mostly micropores (<2 nm) and mesopores (2–50 nm).[23] Micropores provide the interface for charge accumulation, while mesopores facilitate ion and electrolyte diffusion.[23,24] Additionally, the porous carbon can be prepared from biomass materials which are renewable and low-cost. Numerous types of biomass such as

[a]Department of Industrial Engineering, Faculty of Engineering, Ubon Ratchathani University, Ubon Ratchathani, 34190, Thailand. E-mail: santamon.l@ubu.ac.th; Tel: +66 935397469

[b]School of Bio-Chemical Engineering and Technology, Sirindhorn International Institute of Technology, Thammasat University, Pathum Thani, 12120, Thailand

[c]Department of Applied Physics, Faculty of Sciences and Liberal Arts, Rajamangala University of Technology Isan, Nakhon Ratchasima, 30000, Thailand

[d]Department of Chemical Engineering, Faculty of Engineering, Ubon Ratchathani University, Ubon Ratchathani, 34190, Thailand

[e]School of Energy Science and Engineering, Vidyasirimedhi Institute of Science and Technology, Rayong, 21210, Thailand

† Electronic supplementary information (ESI) available. See DOI: https://doi.org/10.1039/d3ra03152g

peanut bran,[25] corncob,[26] lotus seedpods,[27] pea skin,[28] Houttuynia,[29] bamboo,[30] water hyacinth leaves,[20] walnut shell,[31] orange peels,[32] *etc.* are used as carbon precursors for producing porous carbon. The specific area of the carbon prepared from these biomass materials is *ca.* 700–1650 m^2 g^{-1}.[20,25–32] However, these biomass materials are not vastly available in Southeast Asia and do not potentially create an economic valorisation. Also, the carbon synthesis is performed at high temperatures (700–1000 °C). Thus, searching for feasible biomass which is cheap, easily accessible and obtained from economic plants is necessary.

Oil palm is one of the economic plants in Southeast Asia. The oil palm plantation generates great quantities of waste, especially oil palm leaves; they are discarded on the land and sometimes burned in the agricultural area. In Thailand, more than 10 million tons of oil palm leaves per year have not been utilised.[33] The oil palm leaves are rich in lignocellulose and can be used as a carbon source for the synthesis of porous carbons.[34] Hence, it has a great potential to increase the value of the oil palm leaves by using them as carbon precursors in this work. Also, in previous studies, the carbon materials were mostly prepared *via* a step of high-temperature carbonisation (1000–1400 °C). This method is a high energy-consuming and cost-ineffective. An alternative approach such as hydrothermal carbonisation (HTC) has been employed in this work to synthesise the carbon since HTC is facile and has low energy consumption; it operates at medium temperature (160–250 °C) and uses water as a reaction medium.[35,36]

Yet, another simple approach to improving the energy density of supercapacitors is the use of appropriate electrolytes. High-voltage organic electrolytes are widely used for increasing energy density.[37–39] However, they are toxic, highly flammable and volatile.[7] These problems can be addressed by employing an aqueous electrolyte. Although aqueous electrolyte is non-flammable and environmentally feasible,[40] the working voltage is limited by the water splitting reaction at around 1.23 V.[41] The trendy superconcentrated electrolytes, so-called "water-in-salt" (WIS) electrolytes, have been studied to tackle the limited voltage of aqueous electrolytes. The WIS electrolyte was first introduced by Suo *et al.*[42] Superconcentrated lithium bis(trifluoromethanesulfonyl) imide (LiTFSI) was used as an electrolyte for lithium-ion batteries, thereby the stability voltage window can be expanded to 3.0 V. In such a high concentration condition, the hydrogen and oxygen evolution reactions are suppressed due to small numbers of free water molecules.[42,43] Moreover, the reduction of the H_2O/Li^+ molar ratio strongly affects the solvation structure of the electrolyte.[44] The concept of the WIS electrolyte was also applied to supercapacitors by Bélanger's and many research groups to enhance energy density.[45–48] For instance, Hasegawa *et al.* prepared carbon monolith-based supercapacitors with 5 M LiTFSI. The symmetric supercapacitor can operate at 2.4 V and deliver an energy density of 24 W h kg^{-1}.[47] Other high solubility salts such as sodium perchlorate ($NaClO_4$),[49] potassium fluoride (KF),[50] sodium nitrate ($NaNO_3$)[51] and lithium chloride (LiCl)[52] could also act as WIS electrolytes. The use of superconcentrated $NaClO_4$ in supercapacitors, for example, could expand the

voltage window up to 2.30 V.[49] Therefore, WIS electrolytes have been an interesting electrolyte choice for employing in porous carbon-based aqueous supercapacitors. To our best knowledge, hierarchical porous carbon prepared from oil palm leaves and applied as an electrode in WIS based supercapacitor have not been reported before. The effect of porous carbon properties and the types of salt on the performance of the aqueous supercapacitors is rarely discussed.

In this work, oil palm leaf-derived hierarchical porous carbon was prepared using hydrothermal carbonisation coupled with KOH activation (Fig. 1). The weight ratio of KOH/carbon was varied in order to modify the porosity of the carbons. The obtained carbon successfully possessed a developed structure with ultrahigh porosity containing numerous micropores and mesopores. The oil palm leaf-derived hierarchical porous carbon demonstrated an extremely high specific surface area of up to 1928.85 m^2 g^{-1}. The electrochemical performance of the porous carbon-based supercapacitors was studied in two different types (anions) of water-in-salt electrolytes (LiTFSI and LiCl). With the use of the appropriated WIS electrolyte, the potential window of the supercapacitors was expanded to 2.6 V (20 m LiTFSI). However, the oil palm leaf-derived hierarchical porous carbon showed the highest specific capacitance of 331.40 F g^{-1} with the window voltage of 1.9 V when using 20 m LiCl as the electrolyte. These results demonstrated the influence of the concentrated anions on the electrochemical performance of the porous carbon electrode. Hence, such excellent capacitive performance confirms the potential to use oil palm-derived porous carbon as an effective electrode in high-voltage aqueous supercapacitors.

2. Experimental section

2.1. Materials and chemicals

Oil palm leaves (containing 7% of ashes which are 5.91% of Si, 0.45% of Ca, and 0.36% of Mg, Fig. S1†) were collected from a local plantation in Nakhon Ratchasima, Thailand. All the chemicals were analytical grade and used without further purification. Potassium hydroxide (KOH, 85%) was purchased from LobaChemie. Nitric acid (HNO_3, 69.0%), ethyl alcohol (C_2H_5OH, 99.9%) and hydrochloric acid (HCl, 37%) were purchased from J.T.Baker, Reagents Duksan and Merck, respectively. Carbon black Super P (99.9%), polyvinylidene fluoride (PVDF) and 1-methyl-2-pyrrolidone (C_5H_9NO or NMP, 99.5%) applied for electrode preparation were purchased from Alfar Aesar, Sigma Aldrich and QReC, respectively. Lithium trifluoromethanesulfonyl (LiTFSI, ≥99.0%) and lithium chloride (LiCl, 99.99%) from KEMAUS were used as electrolytes for the electrochemical supercapacitor study.

2.2. Synthesis of carbon materials

2.2.1. Pre-treatment of oil palm leaves. In order to remove unwanted impurities, oil palm leaves were soaked in 1 M HNO_3 for 1 h before being washed with deionized (DI) water until its pH stables at around 7. The clean oil palm leaves were then dried in an oven (Memmert, Germany, UN30) at 105 °C for 4 h.

Fig. 1 Schematic illustration of the synthesis of oil palm leaf-derived hierarchical porous carbon.

Finally, the oil palm leaves were ground into powders using a ball mill machine (FRITSCH, Planetary Ball Mill) at 350 rpm for 1 h.

2.2.2. Hydrothermal carbonisation. Firstly, 10 g of oil palm powder was added to 100 ml of 0.5 M HNO_3. The dispersion was transferred into a Teflon-lined stainless-steel autoclave. The autoclave was then placed in an oven at 220 °C for 8 h. After that, the solid was collected by filtration and washed thoroughly with DI water and ethanol several times. Eventually, the sample was dried in an oven at 100 °C for 4 h. The obtained product was abbreviated to OPL_HTC.

2.2.3. KOH activation. The OPL_HTC was mixed with KOH in which a weight ratio of the OPL_HTC (g) : KOH (g) was 1 : 1, 1 : 2 and 1 : 3. Subsequently, the mixture of OPL_HTC/KOH was put in a tubular furnace (Carborite, Stf 16/450) and heated at 800 °C for 1 h. After cooling to room temperature, the sample was washed with 1 M HCl and DI water until its pH reached a value of 7. The sample was lastly dried at 100 °C for 4 h. The final products were denoted as OPL_KOH11, OPL_KOH12 and OPL_KOH13 based on the ratio of OPL_HTC and KOH.

2.3. Material characterisation

To study the morphology of the sample, a scanning electron microscope (SEM, JEOL, JSM-7610F Plus) equipped with an energy-dispersive X-ray spectrometer (EDX, Oxford Instrument) was conducted. X-ray diffractometer (XRD, Bruker) was performed using Cu K_α radiation (λ = 1.54056 Å) in order to examine the structure of as-prepared materials. The nitrogen adsorption–desorption isotherms were acquired at 77 K using

a surface area pore size analyser (Micromeritics, 3Flex). The specific surface area of the samples was calculated using the Brunauer–Emmett–Teller (BET) method. The Barrett–Joyner–Halenda (BJH) pore size distribution was determined from the nitrogen desorption isotherms of the samples. Raman spectra were acquired from a dispersive Raman spectrometer (SEN-TERRA, Bruker) equipped with a 532 nm laser to excite the sample. The X-ray photoelectron spectroscopy (XPS) measurements were performed at the Synchrotron Light Research Institute of Thailand (SLRI). The surface chemistry of the prepared materials was characterized by XPS measurements with a hemispherical analyzer using photon energies between 40-160 and 240–1040 eV at the BL3.2Ua beamline. The photon energy exiting was used at 600 eV for this work. The atomic concentrations were calculated by using RSFs based on Scofield cross-sections.

2.4. Electrochemical measurements

2.4.1. Electrode preparation. In order to prepare the working electrode for a three-electrode measurement, the slurry was prepared by mixing the samples with carbon black and PVDF with a weight ratio of 8 : 1 : 1 in NMP. The slurry was then sonicated in the ultrasonic bath (GT SONIC, D6, 40 kHz) for 30 min. The droplet of the sonicated slurry was carefully dropped on the centre of the glassy carbon electrode (GCE, 2 mm of diameter) surface before being dried in an oven for 1 h. The areal mass loading of active electrode material was ∼1.3–0.5 mg cm^{-2}. Note that, the GCE was previously scrubbed on a cloth with alumina powder (0.3 microns) for 5 min. The electrode

used for full cell testing was fabricated by casting the slurry onto a commercially available aluminium current collector. Two carbon electrodes, prepared similarly with a diameter of 10 mm and approximately equal mass loading ($\sim$2 mg cm^{-2}), were used as the working and counter electrodes in the assembled coin cell (CR 2016). The cell also included a hydrolysed polyethylene (HyPE) separator (thickness of 25 μm, purchased from GELON LIB Group, China) and a WIS electrolyte containing LiCl and LiTFSI.
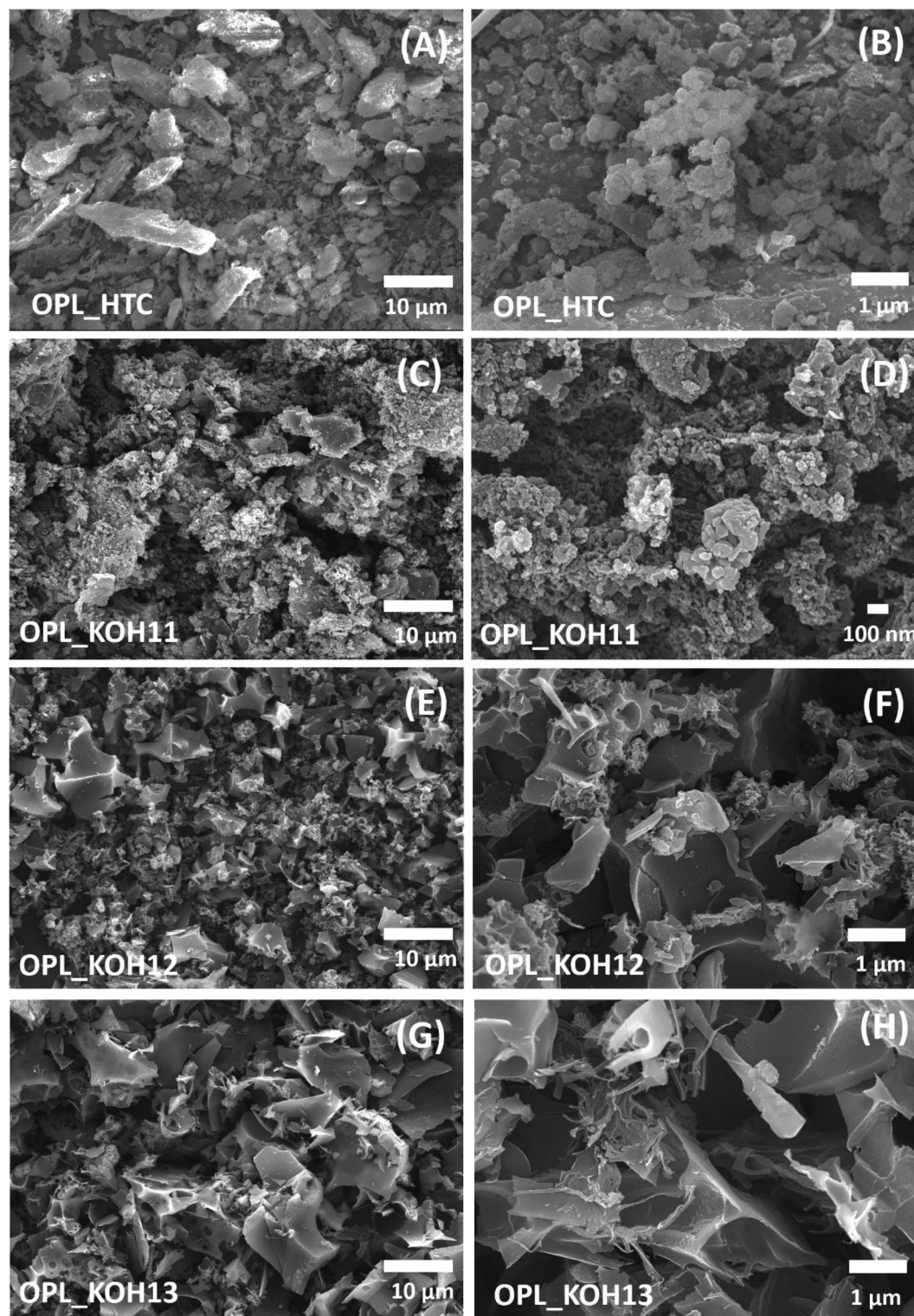

Fig. 2   SEM images of (A and B) OPL_HTC, (C and D) OPL_KOH11, (E and F) OPL_KOH12, (G and H) OPL_KOH13.

2.4.2. Electrochemical evaluation. All the electrochemical tests in the three-electrode configuration were carried out at controlled room temperature (25 °C) using Metrohm Autolab (PGSTAT302N), running NOVA software 2.1. GCE coated with the samples was used as the working electrode, while polycrystalline platinum wire and Ag/AgCl electrode (with double junction) worked as a counter electrode and a reference electrode, respectively. The electrochemical measurements were performed in LiTFSI and LiCl electrolytes (water as a solvent) and two different concentrations of the electrolyte (1 m and 20 m) were applied. The electrochemical performance of the samples was examined using cyclic voltammetry (CV) and impedance spectroscopy (EIS). The scan rate of the CV measurement varied from 5 to 100 mV s^{-1}. The specific capacitance (C_s, F g^{-1}) was calculated from the cyclic voltammetry measurement using the following equation:

$$C_s = \frac{(\int I \, dv)}{(vm \, \Delta V)} \tag{1}$$

where C_s is the specific capacitance, $\int I \, dv$ is the half area of the corresponding CV curve, v is the scan rate (mV s^{-1}), m is the mass of active material (g) and ΔV is the voltage window (V). The EIS test was evaluated at an applied voltage of 0–1.2 V with an amplitude of 10 mV over the frequency range from 100 kHz to 0.01 Hz. For the two-electrode measurement, the galvanostatic charge discharge (GCD) technique (BTS4000) was performed to evaluate the cell performance. The specific capacitance in often calculated from a galvanostatic charge discharge curve by using equation:

$$C = \frac{4I\Delta t}{m\Delta V}$$

where, I is the applied current (A), Δt is discharge time (s), m is the total mass of active material in both carbon electrodes (g), and ΔV is the potential window of the discharging process (V).

3. Results and discussion

3.1. Morphology of oil palm leaves-derived carbon

The morphology of the samples was investigated by scanning electron microscope (SEM). The oil palm leaves without carbonisation shows a smooth surface composed of cellulose (Fig. S2†). After the hydrothermal carbonisation, the OPL_HTC presents coalesced structure (Fig. 2A and B). The irregular shape of the OPL_HTC indicates the distorted cellulose structure of the oil palm leaves which convert to carbon in the hydrothermal reaction. All samples after the KOH activation confirms the critical role of KOH in creating a porous structure as shown in Fig. 2B–H. The OPL_KOH11 exhibits the network structure with pores (Fig. 2C and D). When increasing the ratio of KOH, a flaky structure is formed. The interconnected sheet-like structure can be clearly observed in OPL_KOH12 (Fig. 2E and F). However, the OPL_KOH13 exhibited a smaller size of the flakes compared to OPL_KOH12 (Fig. 2G and H). The breakage of the large sheet into small pieces is related to the continuous reaction between carbon atoms and KOH.[53–56] These interconnected forms of the samples possess open pores for rapid ion diffusion and reduce the resistance of ion transport leading to the high electrochemical performance.[57,58] The SEM-EDX mapping and the elemental composition of all samples also illustrates the lowest amount of oxygen content in OPL_KOH12 compared to other as-prepared carbon materials indicating less oxygen functional groups on the material (Fig. S3†).

3.2. Structure of the as-synthesised porous carbon

The nitrogen adsorption and desorption measurements were employed to study the porosity of the as-prepared carbon. As shown in Fig. 3A, OPL_HTC shows type III adsorption–desorption isotherm attributing to the physisorption on macroporous materials. However, all OPL_KOH samples exhibit mixed type I and IV isotherms confirming the development of other pore types after the KOH activation. The combination of type I/IV adsorption–desorption isotherms indicates the coexistence of micropores and mesopores in the material structure.[59] This result differentiates from most activated porous carbon which typically has a microporous structure with a typical type I.[24] All OPL_KOH materials also possess an obvious type-H4 hysteresis loop which suggests the slit-shaped pore.[45] The pore size distributions of the as-prepared carbon are shown in Fig. 3B. The OPL_KOH materials consist of a large number of micropores, mesopores and a few amounts of macropores, while only mesopores and macropores are found in OPL_HTC. The calculated BET surface area, average pore diameter and pore volume are presented in Table 1. The OPL_KOH13 exhibits the highest BET surface area of 1928.85 m^2 g^{-1} compared to OPL_KOH12 (1840.51 m^2 g^{-1}) and other oil palm-derived carbons from the previous works (685–1685 m^2 g^{-1}).[60–62] The BJH average pore diameter of OPL_KOH samples is in the range of 4.42–2.74 nm due to the pore formation after KOH activation. Interestingly, the OPL_KOH12 exhibits the largest pore volume of 1.16 cm^3 g^{-1} in agreement with the highest absorbed amounts of gases (as seen in the isotherm, Fig. 3A); this could be due to the large amounts of mesopores presented in the OPL_KOH12. In contrast, the micropores mainly contribute 58.18% of the total volume in OPL_KOH13, and only 14.91% and 24.39% of the total volumes ascribed to micropores in OPL_KOH12 and OPL_KOH11, respectively.

The structure of the as-prepared materials is further investigated by X-ray diffraction. All samples present two broad diffraction peaks at around 24° and 43°, corresponding to the (002) and (100) planes of graphite, respectively (Fig. 3C).[27,57,58,63] It is clear that the peaks become weaker and almost faded when the amount of KOH is higher. The XRD patterns of the carbon materials are similar to that of the commercial activated carbon (Fig. S4†). Therefore, these results confirm the less ordered graphitic structure of the as-synthesised carbons.[50,63] Additionally, the high intensity of the small angle diffraction peaks demonstrates the microporous structure of the materials.[59] The calculated interlayer distance of graphitic layers (d_{002}), the thickness of the graphitic domains (L_c) and lateral size of graphitic domains (L_a) are shown in Table 2. The d_{002} interlayer distance of the samples is much higher than that of graphite (0.335 nm)[64] which is expected to be spaces for charge and ion
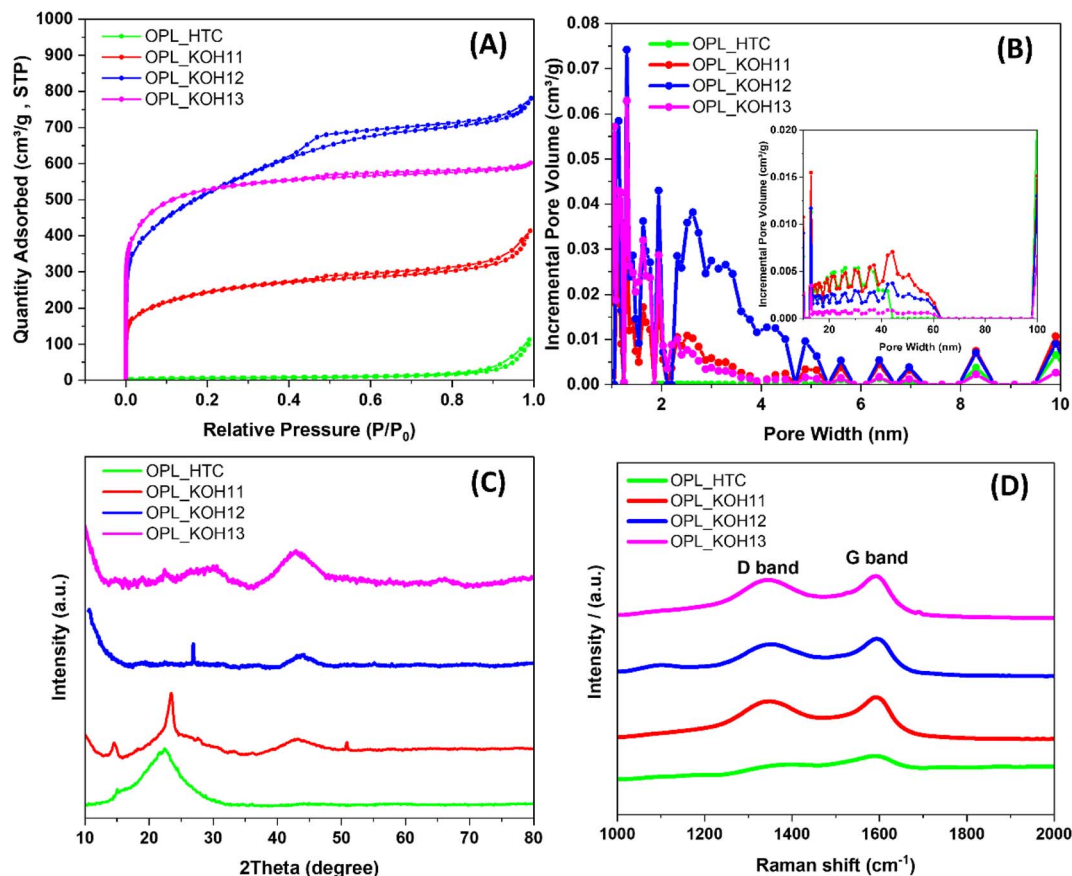
Fig. 3 The structure of the as-prepared samples (A) N_2 adsorption/desorption isotherms, (B) pore size distribution, (C) XRD patterns and (D) Raman spectra.

adsorption leading to high electrochemical performance. The large lateral size is also beneficial to charge storage. Also, the calculated d_{002} and L_c of the OPL_KOH decrease gradually after the activation. The result, therefore, indicates the carbon structure change from short-range ordering to disordering.[65,66]

The degree of graphitisation of the carbon materials was studied by Raman spectroscopy (Fig. 3D). The Raman spectra of all materials possess two broad peaks at around 1346 and 1586 cm^{-1}, which are assigned to the D band (disordered carbon, sp^3 hybridisation) and G band (graphitic carbon, sp^2 hybridisation) respectively.[67] The intensity ratios of the D band and G band are usually used to evaluate the graphitic structure

in carbon materials.[27] The I_D/I_G ratio is 0.75, 0.89, 0.84 and 0.91 for OPL_HTC, OPL_KOH11, OPL_KOH12, and OPL_KOH13, respectively and the lateral size of the graphitic domains (L_a) (Table 2). The result confirms that OPL_KOH12 have the high degree of graphitisation with fewer defects when compared to previous studies.[53,55,61] This result agrees with low oxygen contents in the OPL_KOH12 material as discussed earlier. Moreover, the I_D/I_G ratio of the OPL_KOH is higher with the increase in the KOH ratio. This indicates that the higher amounts of KOH cause intrinsic defects and deterioration of the graphitised structure in the carbon materials.[68] Additionally, the elemental composition of OPL_KOH materials was

Table 1 The pore structure of the as-synthesised carbon

Samples	SSA^a (m^2 g^{-1})			BJH average pore diameter (nm)	Pore volume (V_{total}, cm^3 g^{-1})	Micropore volume (V_{micro}, cm^3 g^{-1})	V_{micro}/V_{total} (%)
	$S_{BET}{}^b$	$S_{micro}{}^c$	$S_{meso}{}^d$				
OPL_HTC	22.33	—	—	25	0.11	—	—
OPL_KOH11	877.63	334.70	542.93	4.42	0.56	0.14	24.39
OPL_KOH12	1840.51	408.23	1432.28	3.22	1.16	0.17	14.91
OPL_KOH13	1928.85	1289.46	639.39	2.74	0.92	0.53	58.18

^{a} SSA: specific surface area. ^{b} S_{BET}: SSA calculated by using the BET model. ^{c} S_{micro}: micropore SSA based on the t-plot method. ^{d} S_{meso}: S_{BET} − S_{micro}.

Table 2 Physical parameters of the as-synthesised carbon

Samples	d_{002} (Å)	$L_c{}^a$ (nm)	$L_a{}^b$ (nm)	I_D/I_G	$L_a{}^c$ (nm)
OPL_HTC	3.93	0.29	—	0.75	0.17
OPL_KOH11	3.81	0.30	0.11	0.89	0.20
OPL_KOH12	3.74	0.09	0.19	0.84	0.19
OPL_KOH13	—	—	0.12	0.91	0.21

^{a} L_c: stacking height of the crystallite, calculated by the equation: $L_c = \dfrac{K\lambda}{\beta \cos\theta}$ ($K = 0.89$, β is half width of (002) diffraction peak, $\lambda = 0.154056$ nm). ^{b} L_a: the lateral size of the crystallite calculated by the equation: $L_a = \dfrac{K\lambda}{\beta \sin\theta}$ ($K = 0.89$, β is half width of (100) diffraction peak, $\lambda = 0.154056$ nm). ^{c} L_a: lateral size of the crystallite calculated by the equation: $L_a = \dfrac{4.4}{I_D/I_G}$.

examined using XPS technique (Fig. S15 and Table S1†). The results confirm the lowest presence of oxygen functional groups on OPL_KOH12 material compared to others which could have a beneficial effect on its electrochemical performance in the water-in-salt electrolyte. These characterization results therefore confirmed the effective HTC method coupled with KOH activation for preparing the excellent quality of hierarchical porous carbon materials from oil palm leaves.

3.3. Electrochemical performance of the samples

In order to examine the electrochemical performance of as-prepared carbons, all samples were first carried out using a three-electrode configuration at room temperature in 1 m LiTFSI electrolyte, also referring to traditional "salts-in-water" (Fig. S5†). Obviously, the electrochemical performance of these carbon electrodes significantly varies, which is mainly attributed to the different pore properties of the materials. The CV curves of OPL_KOH electrodes exhibit a quasi-rectangular shape without any peaks indicating the ideal capacitive behaviour.[68] It is noted that the peak of the oxygen reduction reaction[69,70] could be seen in the OPL_HTC electrode (Fig. S5A†) since it possesses the highest amount of oxygen contents compared to other OPL_KOH electrodes (Fig. S3†); thus, the working potential of the OPL_HTC electrode is relatively narrow. The OPL_KOH12 shows excellent capacitive performance with the highest capacitance of 119 F g^{-1} compared to other carbon materials (Fig. S6†). Interestingly, the potential window of OPL_KOH12 electrodes in 1 m LiTFSI appear to be around 2 V which is higher than the electrochemical stability of water (1.23 V). The widen operating potential accounts for less defects and oxygen-containing functional groups in the OPL_KOH12 which lead to the suppression of water-splitting activity.[50] A pH locally also increases due to the chemisorption of hydrogen/hydroxyls anions in the micropores causing the shift of the hydrogen evolution potential.[48,71] In addition, the EIS results demonstrate the fast ion diffusion and the excellent rate capability of the OPL_KOH12 as seen in the Nyquist plot and the calculated relaxation time (Fig. S7†). Therefore, the superior capacitive performance for OPL_KOH12 can be attributed to the interconnected hierarchical porous structure

and a high fraction of mesopores which facilitate the adsorption and diffusion of electrolyte ions. The OPL_KOH12 also shows the lowest charge transfer resistance confirming the good electrolyte transport of the OPL_KOH12. The as-synthesised carbons were subsequently tested in 20 m LiTFSI to study their electrochemical performance in the "water-in-salt" electrolyte (Fig. S8†). With the use of highly concentrated electrolytes, the operating potential range of the material was also broadened to 2.6 V. The expanded operating potential is corresponded to the restriction of the water splitting reaction due to the scarcity of free water molecules in the 20 m LITFSI electrolyte; almost all water molecules involve the solvation of Li ions. Also, the reduction of the TFSI anions leads to the upshift of the oxygen evolution potential.[48] Similar to the salt-in-water system, the OPL_KOH12 illustrates the best capacitive performance with a capacitance of 176 F g^{-1} in 20 m LiTFSI (Fig. S9†). Similarly, an increase in the specific capacity of the mesoporous hollow carbon nanoplates when using the WIS electrolyte was reported by Quan et al.[72] The enhancement of the electrochemical performance is ascribed to the formation of SEI layers. The scarcity of free water molecules followed by the high concentration of TFSI$^-$ causes the reduction of TFSI$^-$ at the electrode interface.[72]

To study the effect of anions identities on the electrochemistry of the hierarchical porous carbon electrode, the OPL_KOH12 was then tested for its electrochemical properties in LiCl electrolytes. The concentration of the electrolyte is modified from 1 m to 20 m (Fig. S10†). In the same way as the LiTFSI electrolyte, the expanded voltage window is observed when the LiCl electrolyte is highly concentrated (Fig. 4A). However, the operating potential of 20 m LiCl is 1.9 V which is lower than that of 20 m LiTFSI (2.6 V). The result confirms the effect of anion identities in the prepared superconcentrated electrolyte. According to the Hofmeister series, Cl$^-$ anion is stronger in kosmotropes than TFSI$^-$ anion. As the kosmotropes usually compete with water to incorporate into the cation solvation shell, the free water cluster is found and then involved in the water electrolysis of the WIS electrolyte.[73,74] Consequently, the water splitting causes a narrower voltage window of the LiCl electrolyte compared to LiTFSI. Because of the narrow voltage window, the specific capacitance of the electrode in LiCl is higher than in LiTFSI electrolyte (Fig. 4B). The calculated specific capacitance of the OPL_KOH12 is 198 and 331 F g^{-1} in 1 and 20 m LiCl, respectively. In addition, the supplement of cycling properties of OPL_KOH12 in 1 and 20 m LiCl and LiTFSI electrolytes was shown in Fig. S11.†

Furthermore, Trasatti's method was employed to analyse the capacitance in the different electrolytes which was obtained from both the outer surface (easily accessible surface to the electrolyte) and inner surface (pores and grain boundaries)[75,76] (Fig. S11†). It is known that the matching carbon pore size leads to an increase in the specific capacitance. Considering the ion size of hydrated Li$^+$ (0.38 nm),[11] Cl$^-$ (0.32 nm)[66] and TFSI$^-$ (0.79 nm),[77] pores larger than these ion values are accessible to the ions. The total capacitance of OPL_KOH12 in both 1 m LiCl (250 F g^{-1}) and 20 m LiCl (435 F g^{-1}) electrolyte is greater than 20 m LiTFSI (217 F g^{-1}) (Fig. 4C). Since the hydrated Cl$^-$ anion is
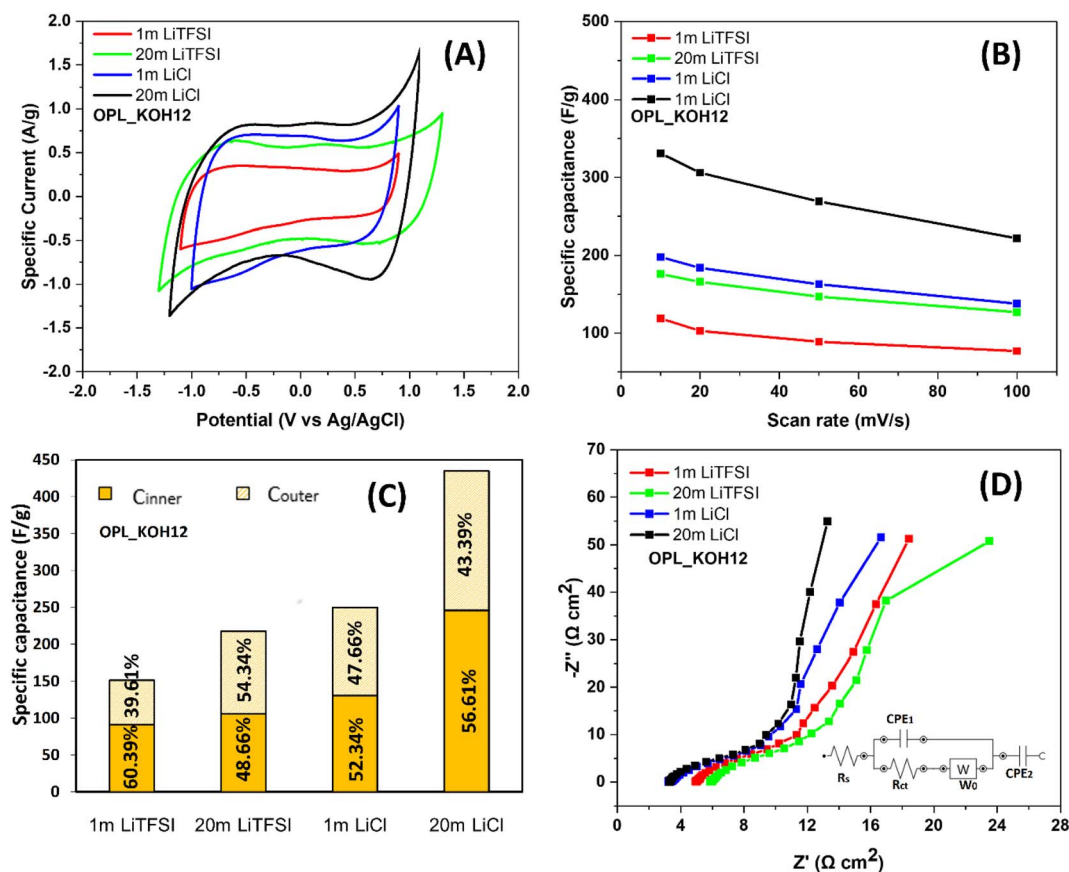
Fig. 4 (A) CV curves of OPL_KOH12 in LiTFSI and LiCl electrolytes (1 and 20 m), (B) the specific capacitance in different electrolytes at various scan rates from 10 to 100 mV s^{-1}. (C) The specific capacitance of the OPL_KOH12 electrode presenting the total capacitance acquired at a very low scan rate and the outer capacitance acquired at a very high scan rate. The inner capacitance was calculated from the difference between C_T and C_{outer} ($C_T = C_{outer} + C_{inner}$), based on the Trasatti method.[76] (D) Nyquist plots of the OPL_KOH12 in LiTFSI and LiCl electrolytes (1 and 20 m).

smaller than TFSI$^-$ and has high ionic conductivity, the Cl$^-$ ion thereby easily accesses the micropores of OPL_KOH12 leading to the relatively high specific capacitance.[11,78] The total capacitance in 20 m LiCl accounts for 56.61% of inner capacitance, confirming the easy accessibility of both cation and anion in the porous structure of the OPL_KOH12. Also, the inner capacitance is independent of the concentration of LiCl electrolyte since the percentage of C_{inner} in 1 m LiCl (52.34%) is not considerably different from that in 20 m LiCl. Thus, the change in the size and solvation sheath of ions in the LiCl$^-$ WIS electrolyte does not extremely influence the ability of ions to diffuse into the pores. The Cl$^-$ anions in both diluted and WIS electrolyte is fairly tidy for penetrating the structure of hierarchical porous carbon. In contrast, the inner capacitance is 48.66% and 60.38% in 20 m and 1 m LiTFSI electrolytes, respectively. This may be due to the Li$^+$ is not desolvated due to its low H$_2$O/Li$^+$ molar ratio and high solvation energy in the WIS electrolyte. Also, two TFSI anions could be found in each Li$^+$ solvation sheath in highly concentrated LiTFSI electrolyte.[42] The ions are then bulky and hardly penetrate the porosity of OPL_KOH12. At high frequencies (Fig. 4d), the equivalent series resistance is related to the sum of the electrolyte resistance outside the pores, the electrode resistance and the contact resistance

between the electrode and the current collector.[79,80] The high ESR of the electrode is correlated to the utilisation of poor conductively glassy carbon as a support and the inferior contact between the material and the glassy carbon surface. The initial resistances of OPL_KOH12 are 6.20 Ω cm^2 and 3.41 Ω cm^2 for 20 m LiTFSI and 20 m LiCl electrolytes, respectively. Since the electrode and the contact resistances same in all systems, the ESR of the electrode in LiTFSI affirms the low ionic conductivity of TFSI$^-$ anion.[78] The viscosity of the LiCl WIS electrolyte is also remarkably less than that of the LiTFSI indicating the lower ionic transporting of Li ions.[81] However, the electrolyte resistance in 20 m LiTFSI is higher than that in 1 m LiTFSI (5.22 Ω cm^2). This is due to the poor wettability (hydrophobic)[50] and high viscosity of the WIS electrolyte.[47,82] The nearly vertical line at low frequencies which defined as the Warburg diffusion region also confirmed the fast ion diffusion of the LiCl electrolyte within the carbon porosity. The ESR and Warburg resistances from the fitting equivalent circuits are shown in Table S2.† In addition, the capacitive performance of the OPL_KOH12 in the WIS electrolyte is approximately equal to or even superior to that of other biomass carbons in aqueous electrolytes, as demonstrated in Table 3.

Table 3 Comparison of the specific capacitance of the as-prepared carbon materials with previously reported biomass-derived carbon material

Raw material	Electrolyte	Potential range (V)	S_{BET} (m^2 g^{-1})	Specific capacitance (F g^{-1})	Reference
Oil palm	1 M H$_2$SO$_4$	0 to 0.5	639.84	52	62
Peanut bran	3 M KOH	0 to 0.9	2565	188	25
Corncob	6 M KOH	−1 to 0	2998	258	87
Bean dregs	6 M KOH	−1 to 0	2313.3	321.3	88
Rubberwood-sawdust	1 M LiTFSI	1.8	1932	100	71
Pea skin	1 M LiTFSI	0 to 2	1828.6	141.1	28
Waste palm	PVA/LiCl	−0.4 to 0.4	1573	226	89
Wheat-straw	PVA/LiCl	−0.4 to 0.4	1905	268.5	90
OPL_KOH12	**20 m LiTFSI**	**−1.3 to 1.3**	**1840.5**	**176.36**	**This work**
OPL_KOH12	**20 m LiCl**	**−1 to 0.9**	**1840.5**	**331.40**	**This work**

As seen in Fig. 5A, the phase angles of the OPL_KOH12 electrode are 65.14° and 76.41° in 20 m LiTFSI and LiCl electrolytes, respectively. The lower phase angle of the electrode in the LiTFSI electrolyte is referred to as the higher resistive properties in the LiTFSI water-in-salt electrolyte.[75] Besides, the characteristic frequency at 45° is known as the knee frequency (f_0) and the relaxation time ($\tau_0 = 1/f_0$) is the minimum time needed to discharge stored energy.[55,83] The lower relaxation time of OPL_KOH12 in 20 m LiCl electrolyte (12.89 seconds) compared to 20 m LiTFSI electrolyte (21.29 seconds) suggests the superior rate capability of the electrode in the LiCl electrolyte. The frequency of the transition region from the resistor to the capacitor of OPL_KOH12 in LiCl electrolytes is higher than that in LiTFSI electrolytes, also confirming the faster Li$^+$ and Cl$^-$ ion diffusion into the pores of carbon material (Fig. 5B).[84–86] Noticeably, the transition frequency is slightly increased when
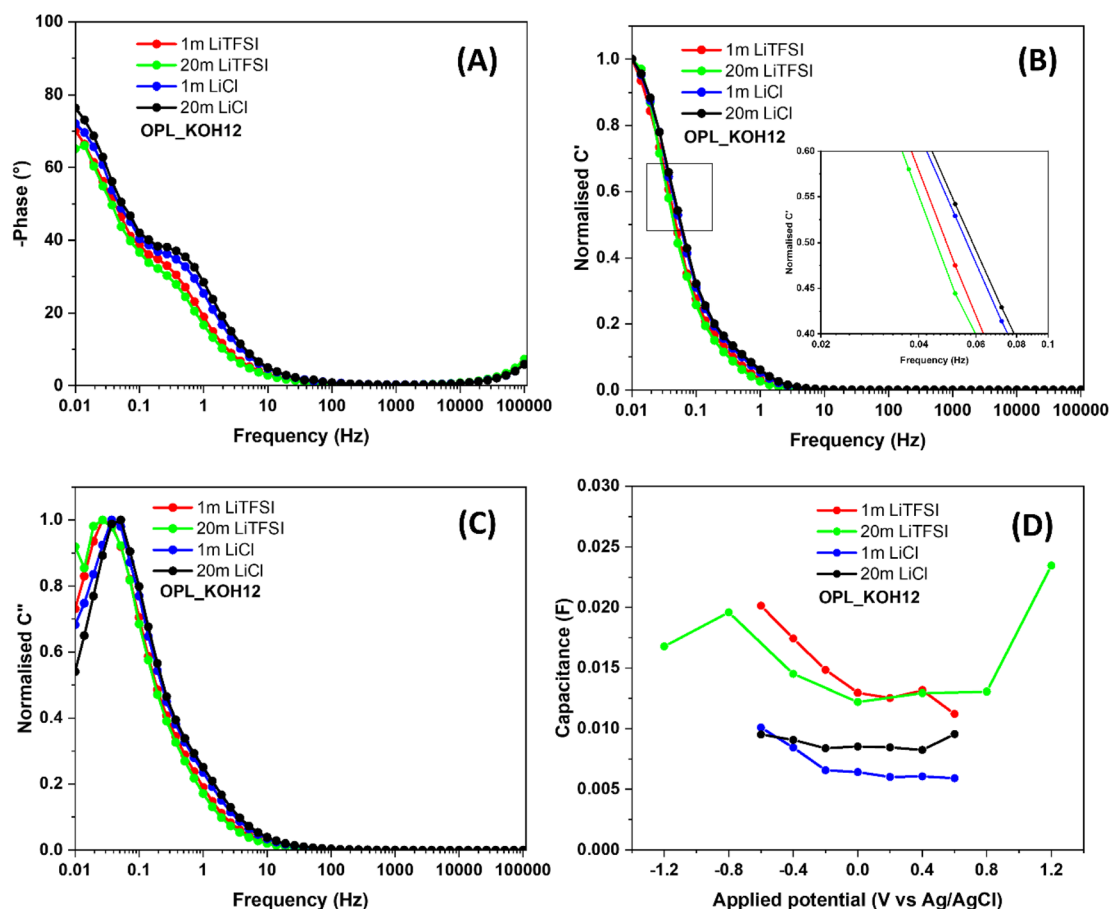

Fig. 5 (A) Bode plots of OPL_KOH12 (all results are tested in 1 m, 20 m LiTFSI and 1 m, 20 m LiCl), (B) real and (C) imaginary parts of the normalized capacitances as a function of frequencies (all above results were tested in different electrolytes), (D) the capacitance of OPL_KOH12 vs. applied voltage in different electrolytes (the capacitance of the electrode was calculated from the EIS measurement using eqn (S3)†).

the LiCl electrolyte becomes highly concentrated (20 m). This could be explained by the similar ionic conductivity between 1 m and 20 m LiCl electrolyte. Recently, Bunpheng *et al.* reported that the ionic conductivity of 20 m LiCl was somewhat higher than that of 1 m LiCl.[81] In addition, the change in size and the solvation sheath are not significant due to the small Cl anion compared to the large TFSI anion. Thus, the ions of the LiCl electrolyte could easily access the small channel of the carbon electrode. The relaxation time can also be obtained from the maximum C'' at a certain frequency (f_0) (Fig. 5C).[84,86] The lowest τ_0 can be found for the OPL_KOH12 sample with 37.28 and 19.31 seconds in 20 m LiTFSI and LiCl respectively. Hence, the electrode shows more capacitive behaviour with rapid ion diffusion into the porous carbon of the LiCl WIS electrolyte when compared to the LiTFSI WIS electrolyte.

With varying the applied potential in 1 m LiTFSI, the capacitance of the electrode under a positive polarisation (11 mF at 0.6 V) is somewhat lower than that under a negative polarization 20 mF at −0.6 V) (Fig. 5D); this is because TFSI⁻ anions are bulkier than Li cations (size of hydrated Li⁺ is 0.38 nm)[11] which thereby they are inaccessible into the small pores of the positively polarised materials. Noted that, the Li⁺ electrosorption occurs on the electrode during a negative polarization whereas the TFSI⁻ anion is absorbed on the positively polarised electrode and inside the material porosity.[48] However, in a 20 m LiTFSI electrolyte, the capacitance of the positively polarised electrode (24 mF at 1.2 V) is higher than that of the negatively polarised electrode (17 mF at 1.2 V). This occurrence can be explained by the change in the ion features in the WIS electrolyte. When compared to 1 m LiTSFI, the size of Li cations in 20 m LiTFSI become larger than the TFSI⁻ anion size since Li ions are not desolvated and then hardly infiltrate in the micropores of the materials.[10,48] Also, the capacitance slightly dropped when the applied potential is −1.2 V. The result indicates the accessible pores were saturated with Li⁺ (negative polarisation).[10] These phenomena can also be found in LiCl electrolytes. In 1 LiCl electrolyte, the capacitance of the positively polarised electrode (6 mF at 0.6 V) is remarkably less than that of the negatively polarised electrode (10 mF at −0.6 V). Still, due to the change of solvation structure of Li ions in 20 m LiCl electrolyte, the capacitance of the OPL_KOH12 electrode under positive polarisation (9.55 mF) is similar to that under a negative polarization (9.52 mF). Therefore, these findings demonstrate that type of anions and solvation sheath of ions in WIS electrolytes notedly influence on the electrochemical performance of the hierarchical porous carbon. Finally, the cyclic stability of the symmetric coin cells fabricated from the OPL_KOH12 electrode using 20 m LiCl and LiTFSI as electrolytes are displayed in Fig. S14.†

4. Conclusions

In summary, the hierarchical porous carbon was successfully synthesised from oil palm leaves. The hydrothermal coupled with the KOH activation methods were carried out to develop the hierarchical porous structure of the materials. The as-prepared porous carbons were subsequently tested for their

electrochemical performance in two different types of water-in-salt electrolytes (LiTFSI and LiCl). As a result, OPL_KOH12 with 1840 m^2 g^{-1} of the specific surface area shows superior electrochemical performance compared to other as-prepared carbon materials due to the suitable pore size for ion diffusion and a high fraction of mesopores in its structure. Using a high-concentrated LiTFSI electrolyte could expand the operating potential window of the OPL_KOH electrode to 1.9 V (LiCl) and 2.6 V (LiTFSI). The narrow voltage window in the LiCl electrolyte is owing to the kosmotropic nature of Cl anion, causing water clusters and then a water-splitting reaction in the system. In addition, the specific capacitance of OPL_KOH12 is 176 and 336 F g^{-1} in 20 m LiTFSI and 20 m LiCl, respectively. With a limited voltage window and smaller anion size of Cl⁻ than TFSI⁻, the specific capacitance of the electrode is higher and mostly attributed to the inner capacitance which refers to the charge storage in the hierarchical pores of the as-prepared carbon. This work also reveals the effect of the ion solvation sheath on the capacitive performance in the water-in-salt electrolyte. Therefore, this finding will be a starting point to further gain insight into the ion sizes dependence of the performance of the hierarchical porous carbons in high-voltage aqueous supercapacitors.

Conflicts of interest

There are no conflicts to declare.

Acknowledgements

References

1 J. R. Miller and P. Simon, Electrochemical Capacitors for Energy Management, *Science*, 2008, **321**(5889), 651–652.

2 M. Winter and R. J. Brodd, What Are Batteries, Fuel Cells, and Supercapacitors?, *Chem. Rev.*, 2004, **104**(10), 4245–4270.

3 N. Kularatna, *et al.*, Supercapacitor-Assisted Techniques and Supercapacitor-Assisted Loss Management Concept: New Design Approaches to Change the Roadmap of Power Conversion Systems, *Electronics*, 2021, **10**, 1697.

4 D. A and G. Hegde, Activated carbon nanospheres derived from bio-waste materials for supercapacitor applications – a review, *RSC Adv.*, 2015, **5**(107), 88339–88352.

5 P. Simon and Y. Gogotsi, Materials for electrochemical capacitors, *Nat. Mater.*, 2008, **7**(11), 845–854.

6 A. González, *et al.*, Review on supercapacitors: Technologies and materials, *Renewable Sustainable Energy Rev.*, 2016, **58**, 1189–1206.

7 L. L. Zhang and X. S. Zhao, Carbon-based materials as supercapacitor electrodes, *Chem. Soc. Rev.*, 2009, **38**(9), 2520–2531.

8 P. Iamprasertkun and R. A. W. Dryfe, The Capacitance of Graphene: From Model Systems to Large-Scale Devices, *Nanocarbon Electrochem.*, 2020, 33–84.

9 A. G. Pandolfo and A. F. Hollenkamp, Carbon properties and their role in supercapacitors, *J. Power Sources*, 2006, **157**(1), 11–27.

10 F. Béguin, *et al.*, Carbons and Electrolytes for Advanced Supercapacitors, *Adv. Mater.*, 2014, **26**(14), 2219–2251.

11 C. Zhong, *et al.*, A review of electrolyte materials and compositions for electrochemical supercapacitors, *Chem. Soc. Rev.*, 2015, **44**(21), 7484–7539.

12 S. Poonam, *et al.*, Review of supercapacitors: Materials and devices, *J. Energy Storage*, 2019, **21**, 801–825.

13 S. Yu, *et al.*, Graphene-based lithium-ion battery anode materials manufactured by mechanochemical ball milling process: A review and perspective, *Composites, Part B*, 2022, **246**, 110232.

14 B. Marinho, *et al.*, Electrical conductivity of compacts of graphene, multi-wall carbon nanotubes, carbon black, and graphite powder, *Powder Technol.*, 2012, **221**, 351–358.

15 C. Liu, *et al.*, Advanced Materials for Energy Storage, *Adv. Mater.*, 2010, **22**(8), E28–E62.

16 B. Hsia, *et al.*, Highly flexible, all solid-state micro-supercapacitors from vertically aligned carbon nanotubes, *Nanotechnology*, 2014, **25**(5), 055401.

17 S. Shiraishi, *et al.*, Electric double layer capacitance of highly pure single-walled carbon nanotubes (HiPco™Buckytubes™) in propylene carbonate electrolytes, *Electrochem. Commun.*, 2002, **4**(7), 593–598.

18 K. Komatsubara, *et al.*, Highly Oriented Carbon Nanotube Supercapacitors, *ACS Appl. Nano Mater.*, 2022, **5**(1), 1521–1532.

19 J. wu, *et al.*, Hierarchical porous carbon derived from wood tar using crab as the template: Performance on supercapacitor, *J. Power Sources*, 2020, **455**, 227982.

20 C. Mo, J. Zhang and G. Zhang, Hierarchical porous carbon with three dimensional nanonetwork from water hyacinth leaves for energy storage, *J. Energy Storage*, 2020, **32**, 101848.

21 A. K. Mishra and S. Ramaprabhu, Functionalized Graphene-Based Nanocomposites for Supercapacitor Application, *J. Phys. Chem. C*, 2011, **115**(29), 14006–14013.

22 J. Zhang and X. S. Zhao, Conducting Polymers Directly Coated on Reduced Graphene Oxide Sheets as High-Performance Supercapacitor Electrodes, *J. Phys. Chem. C*, 2012, **116**(9), 5420–5426.

23 T. Liu, *et al.*, Revitalizing carbon supercapacitor electrodes with hierarchical porous structures, *J. Mater. Chem. A*, 2017, **5**(34), 17705–17733.

24 L. Qie, *et al.*, Synthesis of functionalized 3D hierarchical porous carbon for high-performance supercapacitors, *Energy Environ. Sci.*, 2013, **6**(8), 2497–2504.

25 W. Kang, *et al.*, Peanut bran derived hierarchical porous carbon for supercapacitor, *J. Mater. Sci.: Mater. Electron.*, 2018, **29**(8), 6361–6368.

26 M. Karnan, *et al.*, Electrochemical Studies on Corncob Derived Activated Porous Carbon for Supercapacitors Application in Aqueous and Non-aqueous Electrolytes, *Electrochim. Acta*, 2017, **228**, 586–596.

27 B. Liu, *et al.*, Promising porous carbons derived from lotus seedpods with outstanding supercapacitance performance, *Electrochim. Acta*, 2016, **208**, 55–63.

28 S. Ahmed, A. Ahmed and M. Rafat, Nitrogen doped activated carbon from pea skin for high performance supercapacitor, *Mater. Res. Express*, 2018, **5**(4), 045508.

29 Z. Shang, *et al.*, Houttuynia-derived nitrogen-doped hierarchically porous carbon for high-performance supercapacitor, *Carbon*, 2020, **161**, 62–70.

30 H. Chen, *et al.*, Functional Biomass Carbons with Hierarchical Porous Structure for Supercapacitor Electrode Materials, *Electrochim. Acta*, 2015, **180**, 241–251.

31 X. Xu, *et al.*, Walnut shell derived porous carbon for a symmetric all-solid-state supercapacitor, *Appl. Surf. Sci.*, 2017, **411**, 170–176.

32 M. Dhelipan, *et al.*, Activated carbon from orange peels as supercapacitor electrode and catalyst support for oxygen reduction reaction in proton exchange membrane fuel cell, *J. Saudi Chem. Soc.*, 2017, **21**(4), 487–494.

33 Department of Alternative Energy Development and Efficiency, M.o.E., *Biomass Database Potential in Thailand*, 2012.

34 H. Yang, *et al.*, Biomass-Derived Porous Carbon Materials for Supercapacitor, *Front. Chem.*, 2019, **7**, 274.

35 M.-M. Titirici, Chapter 12 - Hydrothermal Carbons: Synthesis, Characterization, and Applications, in *Novel Carbon Adsorbents*, ed. J. M. D. Tascón, Elsevier, Oxford, 2012, pp. 351–399.

36 Z. Song, *et al.*, Versatile carbon superstructures for energy storage, *J. Mater. Chem. A*, 2023, **11**(24), 12434–12455.

37 G. A. Ferrero, M. Sevilla and A. B. Fuertes, Mesoporous carbons synthesized by direct carbonization of citrate salts for use as high-performance capacitors, *Carbon*, 2015, **88**, 239–251.

38 M. Sevilla and A. B. Fuertes, Direct Synthesis of Highly Porous Interconnected Carbon Nanosheets and Their Application as High-Performance Supercapacitors, *ACS Nano*, 2014, **8**(5), 5069–5078.

39 Z. Lei, *et al.*, A high-energy-density supercapacitor with graphene–CMK-5 as the electrode and ionic liquid as the electrolyte, *J. Mater. Chem. A*, 2013, **1**(6), 2313–2321.

40 L. Miao, *et al.*, Advances in organic cathode materials for aqueous multivalent metal-ion storage, *Mater. Chem. Front.*, 2023, **7**(14), 2731–2749.

41 X. Zang, *et al.*, High-Voltage Supercapacitors Based on Aqueous Electrolytes, *ChemElectroChem*, 2019, **6**(4), 976–988.

42 L. Suo, *et al.*, "Water-in-salt" electrolyte enables high-voltage aqueous lithium-ion chemistries, *Science*, 2015, **350**(6263), 938–943.

43 L. Suo, *et al.*, Advanced High-Voltage Aqueous Lithium-Ion Battery Enabled by "Water-in-Bisalt" Electrolyte, *Angew. Chem., Int. Ed.*, 2016, **55**(25), 7136–7141.

44 L. Coustan, G. Shul and D. Bélanger, Electrochemical behavior of platinum, gold and glassy carbon electrodes in water-in-salt electrolyte, *Electrochem. Commun.*, 2017, **77**, 89–92.

45 X. Liu, *et al.*, Nitrogen-Doped Multi-Scale Porous Carbon for High Voltage Aqueous Supercapacitors, *Front. Chem.*, 2018, **6**, 475.

46 A. Gambou-Bosca and D. Bélanger, Electrochemical characterization of MnO_2-based composite in the presence of salt-in-water and water-in-salt electrolytes as electrode for electrochemical capacitors, *J. Power Sources*, 2016, **326**, 595–603.

47 G. Hasegawa, *et al.*, Hierarchically Porous Carbon Monoliths Comprising Ordered Mesoporous Nanorod Assemblies for High-Voltage Aqueous Supercapacitors, *Chem. Mater.*, 2016, **28**(11), 3944–3950.

48 E. Pameté Yambou and F. Beguin, Effect of salt concentration in aqueous LiTFSI electrolytes on the performance of carbon-based electrochemical capacitors, *Electrochim. Acta*, 2021, **389**.

49 X. Bu, *et al.*, A low-cost "water-in-salt" electrolyte for a 2.3 V high-rate carbon-based supercapacitor, *J. Mater. Chem. A*, 2019, **7**(13), 7541–7547.

50 P. Iamprasertkun, A. Ejigu and R. A. W. Dryfe, Understanding the electrochemistry of "water-in-salt" electrolytes: basal plane highly ordered pyrolytic graphite as a model system, *Chem. Sci.*, 2020, **11**(27), 6978–6989.

51 J. Wang, *et al.*, A Hierarchical Interconnected Nanosheet Structure of Porous δ-MnO_2 on Graphite Paper as Cathode with a Broad Potential Window for $NaNO_3$ Aqueous Electrolyte Supercapacitors, *ACS Appl. Energy Mater.*, 2020, **3**(3), 2614–2622.

52 M. Turgeman, *et al.*, A cost-effective water-in-salt electrolyte enables highly stable operation of a 2.15-V aqueous lithium-ion battery, *Cell Rep. Phys. Sci.*, 2022, **3**(1), 100688.

53 H. Yu, *et al.*, Capacitive performance of porous carbon nanosheets derived from biomass cornstalk, *RSC Adv.*, 2017, **7**(2), 1067–1074.

54 R. Chakraborty, *et al.*, Recent advancement of biomass-derived porous carbon based materials for energy and environmental remediation applications, *J. Mater. Chem. A*, 2022, **10**(13), 6965–7005.

55 X. Liu, *et al.*, Biomass-derived robust three-dimensional porous carbon for high volumetric performance supercapacitors, *J. Power Sources*, 2019, **412**, 1–9.

56 Y. Lv, *et al.*, A comprehensive study on KOH activation of ordered mesoporous carbons and their supercapacitor application, *J. Mater. Chem.*, 2012, **22**(1), 93–99.

57 G. Dhakal, *et al.*, High-performance supercapacitors fabricated with activated carbon derived from lotus calyx biowaste, *Renewable Energy*, 2022, **189**, 587–600.

58 T. K. Das, *et al.*, Nitrogen-doped hierarchically porous carbon obtained *via* single step method for high performance supercapacitors, *Int. J. Hydrogen Energy*, 2022, **47**(26), 12829–12840.

59 J. Guo, *et al.*, Hierarchically Porous Carbon as a High-Rate and Long-Life Electrode Material for High-Performance Supercapacitors, *ChemElectroChem*, 2018, **5**(5), 770–777.

60 S. Nasir, *et al.*, Electrochemical Energy Storage Potentials of Waste Biomass: Oil Palm Leaf- and Palm Kernel Shell-Derived Activated Carbons, *Energies*, 2018, **11**(12), 3410.

61 S. Chanpee, *et al.*, Nanoporous Carbon from Oil Palm Leaves *via* Hydrothermal Carbonization-Combined KOH Activation for Paraquat Removal, *Molecules*, 2022, **27**(16), 5309.

62 R. Taslim, *et al.*, Electrode of supercapacitor synthesized from leaf bunch of oil palm for enhancing capacitive properties, *AIP Conf. Proc.*, 2020, **2219**(1), 050004.

63 X. Zhu, *et al.*, Sustainable activated carbons from dead ginkgo leaves for supercapacitor electrode active materials, *Chem. Eng. Sci.*, 2018, **181**, 36–45.

64 C. Long, *et al.*, Facile synthesis of functionalized porous carbon with three-dimensional interconnected pore structure for high volumetric performance supercapacitors, *Carbon*, 2015, **93**, 412–420.

65 T. Zhang, *et al.*, Pinecone biomass-derived hard carbon anodes for high-performance sodium-ion batteries, *RSC Adv.*, 2017, **7**(66), 41504–41511.

66 Y. Zhu, *et al.*, High-yield humic acid-based hard carbons as promising anode materials for sodium-ion batteries, *Carbon*, 2017, **123**, 727–734.

67 A. C. Ferrari, *et al.*, Raman spectroscopy of amorphous, nanostructured, diamond-like carbon, and nanodiamond, *Philos. Trans. R. Soc., A*, 2004, **362**(1824), 2477–2512.

68 M. Pang, *et al.*, "Water-in-salt" electrolyte enhanced high voltage aqueous supercapacitor with carbon electrodes derived from biomass waste-ground grain hulls, *RSC Adv.*, 2020, **10**(58), 35545–35556.

69 L. Chen, *et al.*, Enabling safe aqueous lithium ion open batteries by suppressing oxygen reduction reaction, *Nat. Commun.*, 2020, **11**(1), 2638.

70 H. Zhang, *et al.*, Crucial role for oxygen functional groups in the oxygen reduction reaction electrocatalytic activity of nitrogen-doped carbons, *Electrochim. Acta*, 2018, **292**, 942–950.

71 E. Le Calvez, *et al.*, High cell-potential and high-rate neutral aqueous supercapacitors using activated biocarbon: *In situ* electrochemical gas chromatography, *Electrochim. Acta*, 2019, **313**, 31–40.

72 T. Quan, *et al.*, Unveiling the Formation of Solid Electrolyte Interphase and its Temperature Dependence in "Water-in-Salt" Supercapacitors, *ACS Appl. Mater. Interfaces*, 2021, **13**(3), 3979–3990.

73 D. Reber, *et al.*, Anion Selection Criteria for Water-in-Salt Electrolytes, *Adv. Energy Mater.*, 2021, **11**(5), 2002913.

74 X. Wang, *et al.*, High-voltage aqueous planar symmetric sodium ion micro-batteries with superior performance at low-temperature of −40 °C, *Nano Energy*, 2021, **82**, 105688.

75 N. O. Laschuk, E. B. Easton and O. V. Zenkina, Reducing the resistance for the use of electrochemical impedance spectroscopy analysis in materials chemistry, *RSC Adv.*, 2021, **11**(45), 27925–27936.

76 W. Hirunpinyopas, *et al.*, Insights into binding mechanisms of size-selected graphene binders for flexible and conductive porous carbon electrodes, *Electrochim. Acta*, 2022, **403**, 139696.

77 S.-W. Xu, *et al.*, Temperature-dependent performance of carbon-based supercapacitors with water-in-salt electrolyte, *J. Power Sources*, 2019, **441**, 227220.

78 Y. Wang, *et al.*, Recent Progress in "Water-in-Salt" Electrolytes Toward Non-lithium Based Rechargeable Batteries, *Front. Chem.*, 2020, **8**, 595.

79 C. Portet, G. Yushin and Y. Gogotsi, Electrochemical performance of carbon onions, nanodiamonds, carbon black and multiwalled nanotubes in electrical double layer capacitors, *Carbon*, 2007, **45**(13), 2511–2518.

80 J. Gamby, *et al.*, Studies and characterisations of various activated carbons used for carbon/carbon supercapacitors, *J. Power Sources*, 2001, **101**(1), 109–116.

81 A. Bunpheng, *et al.*, Revisiting the properties of lithium chloride as "water-in-salt" electrolyte for pouch cell electrochemical capacitors, *J. Electroanal. Chem.*, 2023, **944**, 117645.

82 P. Lannelongue, *et al.*, "Water-in-Salt" for Supercapacitors: A Compromise between Voltage, Power Density, Energy Density and Stability, *J. Electrochem. Soc.*, 2018, **165**(3), A657.

83 T. Purkait, *et al.*, High-performance flexible supercapacitors based on electrochemically tailored three-dimensional reduced graphene oxide networks, *Sci. Rep.*, 2018, **8**(1), 640.

84 M. A. Bissett, *et al.*, Comparison of Two-Dimensional Transition Metal Dichalcogenides for Electrochemical Supercapacitors, *Electrochim. Acta*, 2016, **201**, 30–37.

85 P. Chomkhuntod, *et al.*, Scalable 18,650 aqueous-based supercapacitors using hydrophobicity concept of anti-corrosion graphite passivation layer, *Sci. Rep.*, 2021, **11**(1), 13082.

86 L. Borchardt, *et al.*, Revising the Concept of Pore Hierarchy for Ionic Transport in Carbon Materials for Supercapacitors, *Adv. Energy Mater.*, 2018, **8**(24), 1800892.

87 Y. Zhang, *et al.*, Insights into the KOH activation parameters in the preparation of corncob-based microporous carbon for high-performance supercapacitors, *Diamond Relat. Mater.*, 2022, **129**, 109331.

88 X. Wu, *et al.*, Facile preparation of functionalized hierarchical porous carbon from bean dregs for high-performance supercapacitors, *J. Mater. Sci.: Mater. Electron.*, 2020, **31**(1), 728–739.

89 C. Liu, *et al.*, Fast microwave synthesis of hierarchical porous carbons from waste palm boosted by activated carbons for supercapacitors, *Nanomaterials*, 2019, **9**(3), 405.

90 W. Chen, *et al.*, Rapid single-step synthesis of porous carbon from an agricultural waste for energy storage application, *Waste Manage.*, 2020, **102**, 330–339.